Three-dimensional flow in electromagnetically driven shallow two-layer fluids

R. A. D. Akkermans, L. P. J. Kamp, H. J. H. Clercx, and G. J. F. van Heijst
J.M. Burgerscentre for Fluid Dynamics & Fluid Dynamics Laboratory, Department of Applied Physics, Eindhoven University of Technology, P.O. Box 513, 5600 MB Eindhoven, The Netherlands
(Received 17 December 2009; revised manuscript received 14 May 2010; published 24 August 2010)

Recent experiments on a freely evolving dipolar vortex in a homogeneous shallow fluid layer have clearly shown the existence and evolution of complex three-dimensional (3D) flow structures. The present contribution focuses on the 3D structures of a dipolar vortex evolving in a stable shallow two-layer fluid. Experimentally, Stereoscopic Particle Image Velocimetry is used to measure instantaneously all three components of the velocity field in a horizontal plane and 3D numerical simulations provide the full 3D velocity and vorticity fields over the entire flow domain. Remarkably, the experimental results, supported by the numerical simulations, show to a large extent the same 3D structures and evolution as in the single-layer case. The numerical simulations indicate that the so-called frontal circulation in the two-layer fluid is due to deformations of the internal interface. The 3D flow structures will also affect the distribution of massless passive particles released at the free surface. With numerical studies it is shown that these passive particles tend to accumulate or deplete locally where the horizontal velocity field is not divergence-free. This is in contrast with pure two-dimensional incompressible flows where the divergence of the velocity field is zero by definition.

DOI: 10.1103/PhysRevE.82.026314 PACS number(s): 47.27.E−, 47.32.C−, 47.32.Ef

I. INTRODUCTION

Large-scale geophysical flows such as the Earth's atmosphere and oceans can be considered as quasi-two-dimensional (quasi-2D) due to the combined action of background rotation, density stratification, and the limited vertical dimension as compared to the horizontal ones [1]. On smaller scales, the effects of background rotation and stratification do not play an important role. However, the limited vertical dimension $\mathcal{H}$ as compared to the horizontal length scale $\mathcal{L}$ suppresses vertical motions, and the flow is predominantly planar. Examples where the shallowness alone promotes quasi-two-dimensional flow behavior are rivers, channels, and estuaries (see, e.g., [2,3]). Furthermore, two-dimensional (2D) turbulence can be seen as an extremely shallow flow configuration. Therefore, many experiments have been performed in shallow fluid layers to investigate the dynamics of vortices and 2D turbulence, see Refs. [4–10] and [11] for a review.

Despite the shallowness of the flow, deviations from two-dimensionality occur. This is due to the way the flow is generated but also due to friction at the solid bottom, which induces vertical gradients of the velocity field [10]. In shallow fluid layer experiments the interaction of the flow with the no-slip bottom boundary is usually modeled by adding a linear friction term (Rayleigh friction) to the 2D Navier-Stokes equations under the assumption that the vertical variation of a predominantly horizontal flow field is Poiseuille-like [12–14]. However, several studies have recently shown that the existence of this vertical Poiseuille-like profile is questionable [9,10,15].

In the last years the 3D flow structure of elementary vortices in a shallow fluid layer has received considerable attention [9,10,15–19]. For the monopolar vortex without background rotation, numerical studies by Satijn *et al.* [16] revealed the presence of a secondary circulation as a result of the Bödewadt flow (see, e.g., [20,21]).

Similar secondary flows are also expected within the vortices constituting the dipole. However, several other 3D flow structures have been found for propagating dipoles in shallow fluids. Lin *et al.* [17] showed the emergence of a vortex orthogonal to, and just in front of the propagating dipole. This roll-like vortical structure is referred to as the "frontal circulation" [18,19]. In both the experiments by Lin *et al.* [17] and those by Sous *et al.* [18,19] the dipole was created by injecting horizontally a small amount of fluid in the fluid layer. Furthermore, Sous *et al.* [18,19] report that the frontal circulation was not present in experiments carried out in a two-layer fluid (based on qualitative observations).

Recently, Akkermans *et al.* [9,10] confirmed the presence of this frontal circulation in experiments (and numerical simulations) of electromagnetically forced vortex dipoles in a shallow fluid layer. The importance of this roll-like structure was quantified by the magnitude of the horizontal vorticity component of the frontal circulation cell. This horizontal vorticity exceeded the magnitude of the primary vorticity by at least a factor two during its evolution. In addition to the frontal circulation, strong upwelling in the wake of the dipole and axial motion inside the two individual vortex cores of the dipole are present, the latter even oscillating in time [10].

The above mentioned studies concerned flow structures far away from lateral walls. Cieslik *et al.* [22] studied the influence of a lateral wall on the three-dimensionality of the flow for the canonical case of a dipole-wall collision. Remarkably, the influence of the wall on the vertical motion inside the dipolar vortex becomes stronger for decreasing fluid depths, which was attributed to the role of the frontal circulation [22].

Obviously, in a shallow fluid layer the presence of the bottom boundary plays an important role in causing deviations from purely two-dimensional flow behavior. A way to minimize the influence of the solid bottom is to adopt a two-layer fluid setup, consisting of a lighter fluid layer on top of a heavier bottom layer [14,23–25]. The rationale behind

the two-layer setup is that the measurement layer (the top layer) is now shielded from the no-slip bottom by an extra layer (the bottom layer) to minimize the influence of the no-slip bottom on the flow evolution.

The first study employing the two-layer configuration was by Tabeling and co-workers [26] in 1995. They used a stable configuration of two electrolytes. Basically there are three variations possible for the two-layer configuration: (i) two layers of electrolyte in a stable configuration [14,23,26–28], (ii) a layer of fresh water above an electrolyte [24], and (iii) an electrolyte on top of a dielectric fluid (which is immiscible with the electrolyte) [25,29]. The latter configuration has the advantage that molecular diffusion of salt between the two layers is virtually absent. More importantly, higher Reynolds numbers can be achieved without destroying the stratification (due to absence of mixing between the two layers).

The emergence of 3D flow structures in a shallow fluid layer has received considerable attention [9,10,15–19]. However, whether the two-layer configuration is a significant improvement over the single-layer setup remains an open question.

The present paper reports on a detailed study of the vertical motions developing in shallow two-layer flows. Stereoscopic particle image velocimetry (SPIV) has been used for an experimental investigation of the flow induced by a propagating dipole in the top layer of the two-layer fluid. Additionally, 3D numerical simulations have been carried out, which provide the full 3D velocity and vorticity fields over the entire flow domain. Experiments have been performed, where the upper fluid-layer thickness was decreased in steps down to almost 3 mm, mimicking the traditional fluid-layer configuration for 2D turbulence experiments. Remarkably, the same 3D flow structures and a similar evolution was observed in this two-layer setup as was previously found to occur in a single layer. Furthermore, the importance of internal interface deformations on the 3D motions is elucidated. In order to quantify deviations from pure 2D or quasi-2D flow behavior in the present two-layer fluid, we have compared the kinetic energy contained by the horizontal and the vertical motion and we analyzed the horizontal divergence of the flow. For pure 2D flows vertical motion is absent and the horizontal divergence is zero. The profound influence of the three-dimensionality of the flow is illustrated with passive tracer transport at the free surface. Particles concentrate or deplete in regions where the horizontal flow field is not divergence free, in contrast to 2D incompressible flows where it is divergence free by definition.

The paper is organized as follows: In Sec. II the experimental setup and the measurement technique are introduced and in Sec. III the numerical method is briefly discussed. The experimental and numerical results of the dipole evolution during the forcing and the subsequent free-evolution phase are then presented in Sec. IV. Furthermore, the influence of the deformable internal interface on the 3D flow, the effects of decreasing upper fluid-layer thickness, the degree of two dimensionality of the flow, and tracer transport at the free surface are discussed. Finally, in Sec. V the conclusions are summarized.

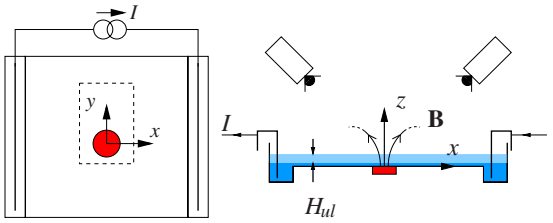

FIG. 1. (Color online) Schematic of the setup for the shallow fluid layer experiments; Left: top view, right: cross section. The electrical current is denoted by I, the fluid depth of the top layer by H_{ul}, and **B** represents the magnetic field produced by the magnet. The field of view is indicated by the dashed rectangle. The x,y,z-coordinate system is also indicated in the figure.

II. EXPERIMENTAL SETUP

The experimental setup used for the two-layer experiments is identical to the setup described in a previous paper (see [10]), except for the fact that now a two-layer fluid system is used. The laboratory setup consists of a shallow two-layer fluid in a stably stratified situation: a denser dielectric lower fluid layer and a lighter conducting upper layer of thickness H_{ul}. In all the experiments the bottom fluid layer depth H_{bl} is kept constant at 3 mm, while the upper layer depth H_{ul} was varied between 3.5 mm and 9.0 mm. The density of the lower fluid (3M™ Novec™ Engineered Fluid HFE-7100) is 1.52×10^3 kg/m^3 (about 1.5 times the density of the electrolyte), and it is immiscible with top layer (thereby excluding vertical mixing between the two layers). The upper layer is a sodium chloride solution (NaCl, 10% Brix), which serves as the conducting fluid enabling the electromagnetic forcing. A disk-shaped magnet is placed underneath the bottom of the tank and an approximately uniform electrical current is led through the top fluid layer, between two electrode plates mounted along opposite side walls. The interaction of the current density and the magnetic field induces a Lorentz force that sets the fluid in motion. Note that the forcing is only active in the top layer. In all the two-layer experiments reported here, the forcing protocol consisted of a 1 s pulse of approximately constant current density ($j_x \approx 0.13$ A/cm^2). The duration of the 1 s current pulse is similar to the duration taken in Paret *et al.* [14]. Furthermore, the Reynolds number at the end of the forcing phase is of similar order as Rivera and Ecke [25].

A schematic of the setup is depicted in Fig. 1. The left-hand side of this figure shows a top view of the 52×52 cm^2 square tank with one disk-shaped permanent magnet below the bottom. Two rectangular-shaped electrodes are placed on opposite sides of the tank, leading to an approximately uniform current density in the x direction. The magnet is placed approximately in the middle of the tank to minimize the influence of the lateral walls and nonuniformities in the current density. Note that the idea of electromagnetic forcing to drive the fluid dates back a long time ago [30]; it was applied in the shallow flow setup to drive the fluid motion, not to two dimensionalize the flow.

We adopt a Cartesian coordinate frame, with the x and y axes spanning a plane parallel to the bottom of the tank, while the z axis is taken vertically upward. The origin of the

coordinate system lies above the center of the magnet on the bottom of the tank. The three velocity components in the x, y, and z direction are denoted by u, v, and w, respectively. The cylindrical magnet, with a diameter of 25 mm and thickness of 5 mm, is assumed to be uniformly magnetized in its axial direction and produces a magnetic field with a magnitude of the order of 1 T.

The right-hand side of Fig. 1 shows a cross-section of the experimental set-up. Two cameras, placed at an angle, enable the use of SPIV [31] to measure the full three-component velocity field in a horizontal plane inside the fluid layer. This horizontal measurement plane is inside the top fluid layer, always at mid-depth of this top layer. The SPIV method consists of a calibration procedure using polynomial mapping functions and a light sheet misalignment correction procedure. The latter utilizes the disparity field to compute the true light sheet position compared to the calibration plane. The measurement images from both cameras are evaluated with a cross-correlation algorithm, and subsequently recombined with the aid of the calibration information (utilizing triangulation) to obtain the three-component velocity field.

The fluid is seeded with polystyrene particles having a mean diameter d_p of 20 μm and a density ρ_p of 1.03×10^3 kg/m^3. Settling of the seeding particles is negligible as the density difference between seeding particles and fluid is small (2%). The volume fraction of the particles is of the order 10^{-5}, so that the seeding particles have a negligible influence on the flow properties. How well these particles follow the flow is characterized by the Stokes number $\mathrm{St} = \tau_p / \tau_f$, where $\tau_p = d_p^2 \rho_p / 18 \mu_f$ is the particle response time to acceleration (μ_f denotes the dynamic viscosity of the fluid). The flow time scale τ_f is estimated as the inverse of the maximum vertical vorticity ≈ 0.07 s, yielding $\mathrm{St} = 3 \times 10^{-4}$, indicating that the particles follow the flow passively.

The seeding particles are illuminated with a dual pulse Nd:Yag laser (Spectron Laser SL454, 200 mJ/pulse), which produces a horizontal light sheet of 1 mm thickness. In order to limit the in-plane particle loss [31] and for correct temporal sampling of the signal, a delay time between laser pulses of 10 ms is chosen.

The illuminated particles are recorded with two cameras (Kodak ES2020 with sensor resolution 1200×1600 pixels, $f_\# = 2.8$), which are mounted on Scheimpflug adaptors to enable in-focus imaging of the entire field of view, as the stereoscopic angle is approximately 85 degrees. The cameras and the light source are synchronized with a delay generator. With this setup, image pairs are acquired at a rate of 15 Hz. The typical field of view is approximately 5.5×7 cm^2 in x and y direction, respectively. The field of view is indicated schematically in Fig. 1 by the dashed rectangle. After post-processing, velocity fields were resolved on a 60×79 spatial grid, corresponding to a grid spacing of approximately 1 mm in both x and y direction.

The goal of these experiments is to analyze and quantify the 3D structures that develop in a shallow two-layer fluid, and to make a comparison between the single and two-layer fluid experiment. In order to study the influence of different fluid-layer depths on the flow behavior, the top-layer thickness H_{ul} has been decreased in steps down to almost 3 mm, i.e., 9, 7, 5, and 3.5 mm. The latter fluid-layer thickness mimics the traditional fluid-layer configuration for 2D turbulence experiments (see, e.g., [14,23,25,29]). Table I provides an overview of the performed experiments. Note that the Reynolds number Re is based on the maximum horizontal velocity $\mathcal{U}$ at the end of the forcing, while the magnet diameter D is taken as a measure of $\mathcal{L}$. The densimetric Froude number Fr is defined as $\mathcal{U}/\sqrt{g' H_{ul}}$. The reduced gravity g' is computed as $g \Delta\rho / \rho_1$, with $\Delta\rho = \rho_2 - \rho_1$ (subscripts 1 and 2 refer to the top and bottom layer, respectively) and g denotes the gravitational acceleration.

TABLE I. Experimental parameter values for the SPIV measurements in the two-layer flow: upper fluid-layer depth H_{ul}, measurement level h_{ls}, current density j_x, Reynolds number Re, and densimetric Froude number Fr. Note that the bottom layer thickness H_{bl} is kept constant at 3 mm for all experiments.

H_{ul} (mm)	h_{ls} (mm)	j_x [a] (A/cm^2)	Re (-)	Fr (-)
9.0	7.5	0.13	1200	0.23
7.0	6.5	0.12	1250	0.28
5.0	5.5	0.13	1700	0.43
3.5	4.5	0.14	2000	0.64

[a]Due to an unfortunate typing error the reported values of j_x in [10] are a factor 10 too high (fortunately, this typing error has no consequences for the experimental and numerical results in [10]). The here presented values are comparable to the corrected values of [10].

All measurements have been performed in a horizontal cross-sectional plane at mid-depth of the top fluid layer. In Sec. IV results are presented mainly for the experiments with $H_{ul} = 7.0$ mm, as the flow evolution observed in these experiments is indicative for the experiments with different fluid-layer depths. The geometrical aspect ratio γ is defined as $\mathcal{H}/\mathcal{L}$, where the magnet diameter D is a measure of the horizontal length scale. The case $H_{ul} = 7.0$ mm ($\gamma = 0.28$) is in agreement with the classical experiments by Tabeling and co-workers [23,27,28] and by Rivera and Ecke [25].

III. NUMERICAL METHOD

The experiments, as described in the previous Section, will be compared with numerical simulations obtained with the commercial software code COMSOL Multiphysics. These simulations are aimed at mimicking the experimental flow situations.

The motion in the two individual fluid layers of the two-layer simulation is governed by the Navier-Stokes equation, i.e.,

$$\frac{\partial \mathbf{v}_i}{\partial t} + (\mathbf{v}_i \cdot \nabla)\mathbf{v}_i = -\frac{1}{\rho_i} \nabla p_i + \nu_i \nabla^2 \mathbf{v}_i + \frac{1}{\rho_i} \mathbf{f}_i \quad \text{in } \mathcal{D}_i, \quad i = 1,2 \tag{1}$$

complemented by $\nabla \cdot \mathbf{v}_i = 0$, where $\mathbf{v}_i$ is the 3D velocity vector, p_i the pressure, ν_i the viscosity, ρ_i the mass density, and $\mathbf{f}_i$ the external body force in layer i. The subscript $i = 1$ in Eq. (1) refers to the top layer, while $i = 2$ indicates the bottom layer.

For the upper layer, the external body force $\mathbf{f}_1$ constitutes of the Lorentz force, which is given by

$$\mathbf{f}_1 = \mathbf{j} \times \mathbf{B}. \tag{2}$$

Here the current density $\mathbf{j}$ is a uniform and constant pulse of 1 s duration in the x direction ($\mathbf{j}=j_0\mathbf{e}_x$ for $0<t\leq 1$ s and $\mathbf{j}=0$ for $t>1$ s), similar to the forcing applied in the experiments. The reader is referred to [10] and references herein for a more detailed description of the modeling of the magnetic field associated with the disk-shaped magnet.

As the magnet's strength is not exactly known, it is adjusted in such a way that the numerical simulation matches the corresponding laboratory experiment at some arbitrary moment in time. For this matching one can use different criteria, such as the maximum of the vertical vorticity component or the "horizontal" kinetic energy, both at the end of the forcing period. The former matching criterion is used for the numerical results presented in the remainder of this paper, as the local magnitude of the vertical vorticity determines the strength (and thus the speed) of the dipole at a certain height inside the fluid.

For the lower layer Eq. (1) is used, with $i=2$. However, as in the two-layer fluid experiments, the fluid is only forced in the upper layer, so that the external body force in this layer is $\mathbf{f}_2=0$.

The no-slip condition is used at the bottom and a rigid, stress-free condition at the free surface. At the internal interface, where the two sets of equations are coupled, kinematic boundary conditions are applied, dictating that the velocity components should be continuous over this interface ($u_1=u_2$, $v_1=v_2$, and $w_1=w_2$), and besides it is assumed that the interface does not deform ($w_1=w_2=0$). Furthermore, a dynamic boundary condition at this interface is applied, stating that the shear and normal stresses should be continuous over the internal interface [1], i.e.,

$$\rho_1\nu_1\frac{\partial v_1}{\partial z} = \rho_2\nu_2\frac{\partial v_2}{\partial z} \quad \text{and} \quad \rho_1\nu_1\frac{\partial u_1}{\partial z} = \rho_2\nu_2\frac{\partial u_2}{\partial z},$$

and

$$2\rho_1\nu_1\frac{\partial w_1}{\partial z} - p_1 = 2\rho_2\nu_2\frac{\partial w_2}{\partial z} - p_2,$$

respectively.

Note that the assumption of a nondeformable free surface and internal interface represents a qualitative difference between the numerical simulations and the experiments, since in the latter case these surfaces are deformable. Free-surface deformations were shown to be of minor importance in generating vertical motions for the single-layer dipole [10]. However, the possible effect of the rigid internal interface will be discussed in the results section. Implementation of a deformable internal interface is currently not feasible in the simulations. However, as this rigid internal interface is the only qualitative difference with the laboratory experiments, these simulations help to elucidate the effect of a movable fluid interface.

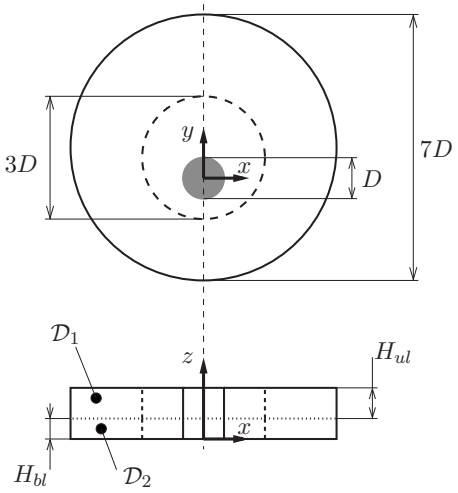

FIG. 2. Schematic top and side views of the computational domain used for the two-layer simulations. $\mathcal{D}_1$ and $\mathcal{D}_2$ refer to the top (having fluid height H_{ul}) and bottom layer (H_{bl}), respectively. The internal interface is indicated with the dotted line in the side view. Note that the vertical dimension of the computational domain is exaggerated for clarity of presentation.

The computational domain is identical to the experimental one with the exception of the lateral (outer) domain boundary (see Fig. 2). This is taken circular (for computational efficiency) with a diameter of 7 times the magnet diameter, whereas the experimental setup has a square outer boundary. It has been checked by simulations with a larger circular domain that its size did not affect the result. The small, solid gray circle in Fig. 2 (top view) represents the domain above the magnet. The outer domain is shifted in the positive y direction as the dipole will be propagating in this direction. The dashed circle represents the border between a fine meshed domain (closer to the magnet) and a domain with a coarser mesh (outer region). Furthermore, use was made of the symmetry in the domain, indicated with the dashed straight line in Fig. 2, i.e., only the right part of the domain was used. For some cases it was checked with a simulation of the full domain that this imposition of symmetry did not affect the result.

To acquire the desired accuracy in a typical run, the computational domain is discretized with approximately 150 000 mesh elements, with finer elements being used near the bottom, near the free surface, and close to the internal interface (where the forcing is strongest) in order to resolve the gradients in the local flow field. With Lagrange elements of degree 2, the resulting number of degrees of freedom solved for is then approximately one million.

As a comparison, the 3D numerical simulation as described above is confronted with a numerical simulation of the 2D Navier-Stokes equation for the evolving dipolar vortex. In this 2D simulation the horizontal component of the Lorentz force present at mid-depth of the top-fluid layer was used to drive the fluid, which produces a dipole having approximately the same Reynolds number at the end of the forcing as in the 3D simulation. The 2D computational domain (having zero thickness) is identical to the top view of Fig. 2. A comparison of tracer transport in these 2D compu-

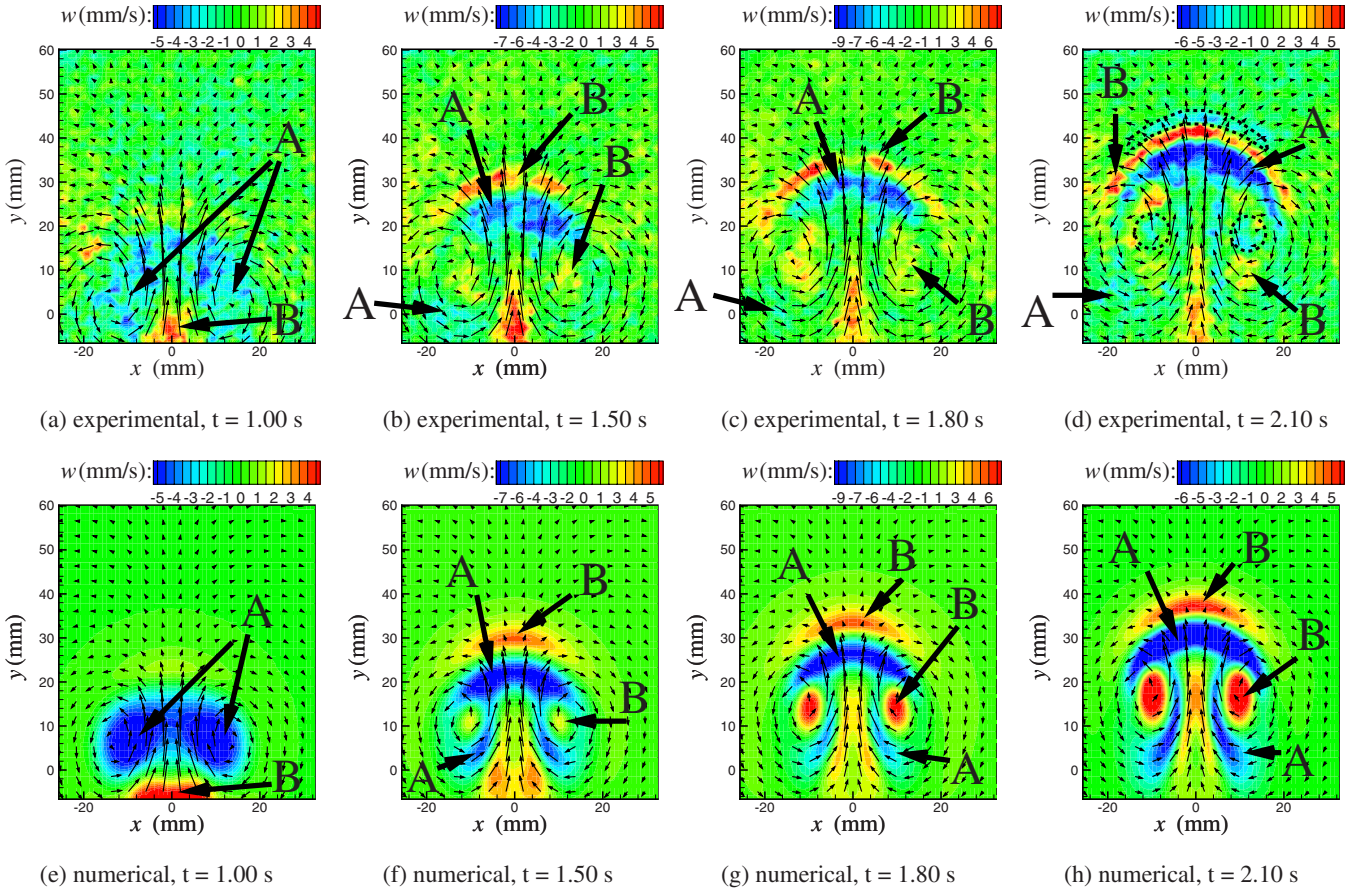

(a) experimental, t = 1.00 s (b) experimental, t = 1.50 s (c) experimental, t = 1.80 s (d) experimental, t = 2.10 s

(e) numerical, t = 1.00 s (f) numerical, t = 1.50 s (g) numerical, t = 1.80 s (h) numerical, t = 2.10 s

FIG. 3. (Color online) Instantaneous velocity fields of a dipolar vortex in a two-layer system observed in a horizontal plane at mid-depth of the top fluid layer (H_{ul}=7.0 mm). Vectors represent horizontal velocity components and color/gray levels indicate the magnitude of the vertical velocity. In these figures, 'A' indicates a region of downward motion ($w<0$) and 'B' an upward motion ($w>0$). Experimental results obtained with SPIV at (a) t=1.00 s, (b) t=1.50 s, (c) t=1.80 s, and (d) t=2.10 s. Numerical snapshots obtained with a rigid internal interface at (e) t=1.00 s, (f) t=1.50 s, (g) t=1.80 s, and (h) t=2.10 s. The dashed circles in (d) indicate the region of downwelling inside the vortex cores (i.e., second sign-change of vertical motion w) and the elongated dashed contour points toward the region of down welling associated with the frontal circulation.

tations with transport in full 3D simulations is intended to illustrate the important effect of 3D recirculating flows on the dispersion of passive tracers (at the free surface).

To investigate the transport behavior of passive particles, the numerically obtained velocity field is integrated in time. The position of a particle at time $t^\star$ is given by

$$\mathbf{x}(t^\star) = \mathbf{x}_0 + \int_0^{t^\star} \mathbf{v} dt, \tag{3}$$

where $\mathbf{x}_0$ is the initial particle position. Integration of Eq. (3) is performed numerically using a fourth-order Runge-Kutta method.

For the 2D simulations, the numerically obtained 2D velocity field is integrated in time with Eq. (3). When releasing particles on the free surface for the 3D simulations, basically a 2D tracking of these particles is performed as the vertical velocity component w is identically zero at the free surface. The difference, however, is that the velocity field of the 2D simulation is divergence free as opposed to the horizontal velocity field at the free surface obtained with the 3D simulation.

For the two-layer dipole simulation (as well as the corresponding 2D simulation), several thousands of particles were released at t=0 on a spatially uniform grid at the free surface, where w=0.

IV. EXPERIMENTAL AND NUMERICAL RESULTS

In this section the experimental and numerical results are presented. First, the experimental results for the case H_{ul} =7.0 mm are discussed, together with the corresponding numerical results (although obtained for the case of a rigid internal interface). Next, the effect of a decreasing upper fluid layer depth is considered. Finally, the transport of passive tracers at the free surface is illustrated.

A. 3D flow evolution of a dipole in a two-layer fluid

Figure 3 shows plots of the instantaneous velocity fields in a horizontal plane at mid-depth of the upper layer. The horizontal velocity components are represented by the vectors. For clarity of presentation the vectors are under sampled: only every fourth vector is shown in the x and in

the y direction, so that (approximately) only 6% of the total set is shown. Since the total forcing time $\Delta t=1$ s and the forcing is started at $t=0$, Fig. 3(a) corresponds to the end stage of the forcing, while Figs. 3(b)–3(d) show the flow field after the forcing has stopped.

During the entire forcing phase, a buildup of downward motion is seen inside the two vortex cores, as is illustrated in Fig. 3(a), as well as strong upwelling in the tail of the dipole. After the forcing has stopped, see Fig. 3(b), the dipole starts to propagate and soon upward motion is seen inside the vortex cores, surrounded by an area with downward motion. At a later stage of the flow evolution, the vertical motion inside the vortices is seen to change in a downward one [delineated by the dashed circles in Fig. 3(d)]. Furthermore, bands of upward and in front of that downward motion are observed at the frontal side of the moving dipole [where the latter is indicated by the dashed contour in Fig. 3(d)], representing the frontal circulation roll. The observed vertical motions are localized in space, and become of comparable order as the horizontal motion. Surprisingly, the 3D structures and evolution as depicted in Figs. 3(a)–3(d) show a remarkable resemblance with the ones already seen in the single-layer dipole (see [10]).

For the dipole in a single-layer fluid, the development of vertical motion was related to vertical gradients in the horizontal flow field [10]. Apparently, the horizontal flow field in the top layer has a z dependence that is similar to the one present in the single-layer case, which explains the close similarity of the 3D structures and evolution in the two-layer fluid. This z dependence is introduced by the magnetic field whose strength varies with height and also by the shear stress exerted by the bottom layer.

Comparison of the numerical simulation results shown in Figs. 3(e)–3(h) with the corresponding experimental observations [Figs. 3(a)–3(d)] reveals a striking resemblance with respect to the flow structures and their evolution. However, there is a slight phase shift present, e.g., the second sign change of the vertical velocity inside the individual vortex cores in the experiment [see Fig. 3(d), indicated by the dashed circles] is not yet seen in the numerical snapshot shown in Fig. 3(h); this occurs after approximately $t=2.5$ s in the simulation. Furthermore, the frontal circulation is not seen in the top layer of the numerical simulation [compare Fig. 3(h) with Fig. 3(d)], the region of rather weak downward motion associated with the frontal circulation [as delineated by the dashed contour in Fig. 3(d)] is not present in the numerical simulation [frontal band of upward motion, see "B" in Fig. 3(h)]. This absence is attributed to the rigid internal interface used in this simulation, as will be explained next.

B. Development of the frontal circulation

The absence of the frontal circulation is illustrated in more detail in the vertical slice presented in Fig. 4(a). The negative vorticity ω_x in the lower fluid layer is associated with the viscous boundary layer at the no-slip bottom. At later stages in the evolution this negative vorticity patch detaches from the bottom and forms the frontal circulation, in a way similar to what is observed in the single-layer situation [see Fig. 4(b)]. However, in the two-layer case this negative vorticity ω_x does not penetrate through the internal interface [indicated with the dashed white line in Fig. 4(a)], and is therefore absent in the top layer. The positive vorticity ω_x is associated with the down welling initiated during the forcing phase (the magnetic field decays with height, which results in a pressure gradient that drives a downward motion). This downward and subsequently horizontal motion is deflected upward at the instantaneous separatrix, the latter is delineated by the band of upward motion in front of the dipole [see, e.g., Fig. 3(f)]. This results in the positive ω_x vorticity patch seen in both the single- and two-layer simulations as indicated by the solid circles in Fig. 4. However, in the two-layer simulation only the upper fluid layer is forced, therefore the positive vorticity patch is only present in the upper layer. Note that the magnitude of the (positive) vorticity component ω_x in the vertical slice of Fig. 4(a) turns out to evolve to significantly larger values than that of the "primary" vorticity component ω_z, like in [10].

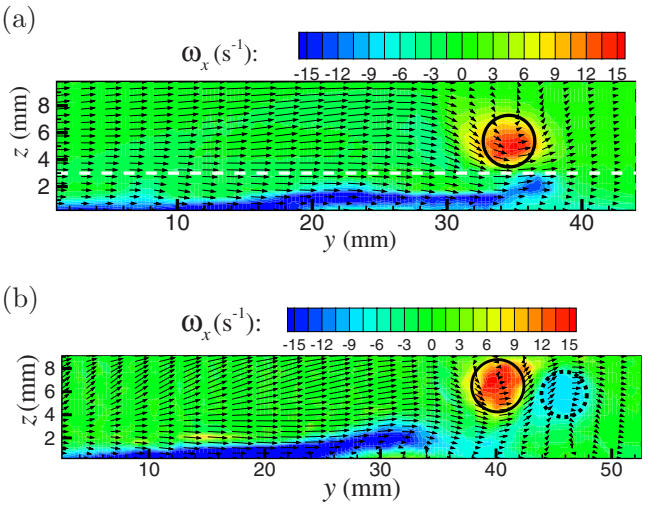

FIG. 4. (Color online) Numerically obtained snapshots of vertical slices through the symmetry plane of the dipole ($x=0$) at time $t=2.60$ s showing the ω_x vorticity distribution, with vectors representing the flow in the yz-plane. Snapshot of (a) two-layer setup, illustrating the absence of the frontal circulation in the top layer (the white dashed line indicates the internal interface between the fluid layers) and (b) single-layer setup with frontal circulation present. The solid and dashed circles indicate the positive and negative ω_x vorticity patches, respectively.

In the numerical simulation the interface is taken flat, whereas in the experiment the interface will most likely deform, as the density of the two fluids is comparable ($\Delta\rho/\rho_1 \approx 0.5$). In the present two-layer experiments the formation of the frontal circulation has presumably a different origin than in the one-layer experiments discussed by Akkermans *et al.* [10], as it is to be directly linked with the interface deformation. Interface deformation implies baroclinic vorticity production, which is described by a source term of the form $\frac{1}{\rho^2}\nabla\rho\times\nabla p$ in the vorticity equation. The sharp internal interface implies locally a strong density gradient. As soon as the interface deforms, the pressure gradient and density gradient are no longer aligned ($\nabla\rho\times\nabla p\neq 0$), which leads to vorticity

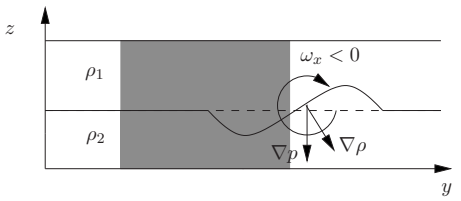

FIG. 5. Schematic illustration of the baroclinic vorticity production resulting from interfacial deformation in a stably stratified two-layer system. The position of the dipole is schematically illustrated in gray.

production. This is schematically depicted in Fig. 5, showing the interface deformation at the front side of the dipole (in the symmetry plane of the dipole, i.e., $x=0$). Based on the simulation, the interface will be displaced upwards at the front and downward closer to the dipole [cf. Figure 3(h)], resulting in the interfacial shape as depicted in Fig. 5. Locally, the density gradient $\nabla\rho$ is directed downwards, perpendicular to the interface. Together with a vertical pressure gradient as shown in the schematic, this leads to a production of negative vorticity ω_x in the top layer. This negative vorticity patch is then advected upward in a way similar to what is seen in the single-layer case [cf. Fig. 4(b)].

Gravity waves at the frontal side of quasi-2D dipoles have been reported in literature related to atmospheric science (see, e.g., [32]). As the interface Froude number in the experiments is fairly high, similar effects may be present in the current two-layer experiment.

C. 3D structure of the dipole with decreasing upper fluid layer depth

Figure 6 shows snapshots of the dipolar flow structure for different upper fluid-layer depths: the panels show the structure of the horizontal and vertical fluid motion in a horizontal cross-section at mid-depth of the top layer for the case of an upper layer thickness (a) $H_{ul}=9.0$ mm, (b) $H_{ul}=7.0$ mm, (c) $H_{ul}=5.0$ mm, and (d) $H_{ul}=3.5$ mm. For all cases one observes a similar pattern of vertical motion, as was also seen for the case $H_{ul}=7.0$ mm [see Fig. 6(b)] that was discussed in Sec. IV A; strong upward motion in the tail of the dipole, together with the frontal circulation. In contrast to the qualitative observation by Sous *et al.* [18,19], the quantitative flow measurements in the two-layer experiments reported here give clear evidence of the frontal circulation. Also, in all four snapshots the second sign change of the vertical velocity inside the individual vortices can be seen. These features are also present for the case $H_{ul}=5.0$ mm, although less pronounced. Clearly, the observed 3D structures in the $H_{ul}=7.0$ mm case are indeed representative for the other upper fluid depths. The same applies for the evolution in time. The magnitude of the vertical velocity component remains approximately constant with decreasing H_{ul}, whereas the horizontal velocity magnitude increases with decreasing upper fluid-layer thickness. This increase is expected as the measurement plane becomes more close to the magnet for decreasing H_{ul}, where the Lorentz force effectively drives a stronger horizontal velocity field. In the next section, numerical simulations are discussed where this effect is studied.

The shallowness of the fluid layers in our experimental setup is often used as a justification for quasi-2D flow behavior. Although the snapshots of the velocity field indicate that the magnitude is almost independent of the fluid depth H_{ul}, it is useful to introduce dimensionless numbers to quantify the shallowness of the flow and to compare these with data from the literature. When the flow is electromagnetically generated, the magnet dimension is a measure of the horizontal length scale $\mathcal{L}$. The geometrical aspect ratio γ is then defined as $\mathcal{H}/\mathcal{L}$, where $\mathcal{H}$ is a measure of the vertical length scale. In Table II the γ range for the performed experiments is presented, as well as some typical literature values. Clearly, the aspect ratio of cases $H_{ul}=9.0$ mm($\gamma=0.36$) and 7.0 mm ($\gamma=0.28$) are consistent with the γ-values of Tabeling and co-workers [23,27,28] and Rivera and Ecke [25]. Furthermore, the case $H_{ul}=3.5$ mm(γ

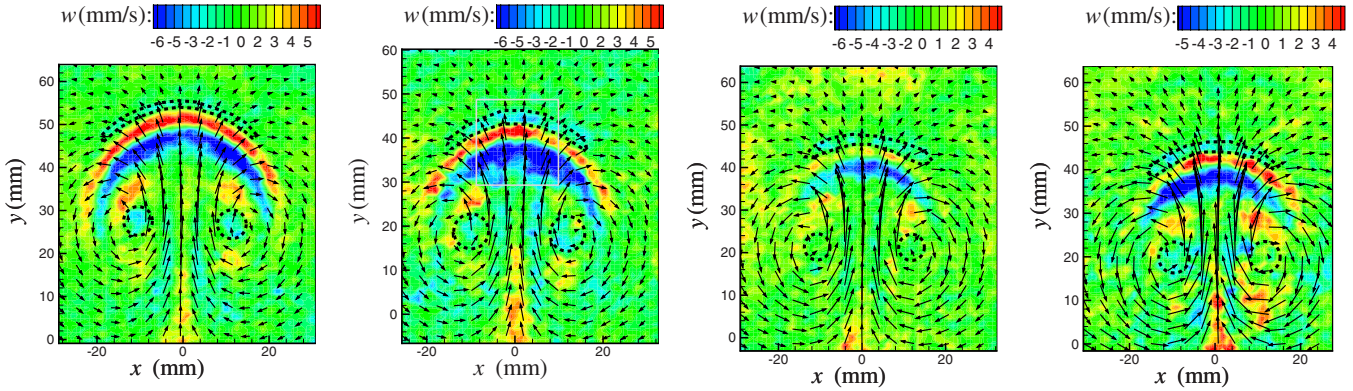

(a) H_{ul} = 9.0 mm (b) H_{ul} = 7.0 mm (c) H_{ul} = 5.0 mm (d) H_{ul} = 3.5 mm

FIG. 6. (Color online) Experimentally obtained velocity fields of a dipolar vortex in a horizontal plane at mid-depth of the top fluid layer having a thickness of (a) $H_{ul}=9.0$ mm, (b) $H_{ul}=7.0$ mm, (c) $H_{ul}=5.0$ mm, and (d) $H_{ul}=3.50$ mm. The time instants have been chosen such that the second sign reversal of vertical velocity inside the vortex cores can be seen as well as the frontal circulation. The solid gray rectangle in (b) indicates the co-moving area over which the "local" ratio q is computed. See caption of Fig. 3 for meaning of dashed circles and contours.

TABLE II. Geometrical aspect ratio $\gamma(=\mathcal{H}/\mathcal{L})$ for the performed two-layer experiments together with literature values. Unless stated otherwise, the cited references employ a stable two-layer fluid setup, with a heavy (dielectric) bottom fluid layer and a lighter conducting top layer.

References	$\mathcal{H}$ (mm)	$\mathcal{L}$ (mm)	γ (-)	Re (-)
Present study	9.0–3.5	25	0.36–0.14	1150–2000
Tabeling *et al.* [23,27,28][a]	3	8	0.375	200–400[b]
Rivera and Ecke [25]	3	12.7	0.24	1200[c]
Shats *et al.* [29]	4	5	0.8	100[d]

[a]The Refs [23,28] utilize a two-layer setup of NaCl solutions with different densities in a stable configuration, i.e., both fluid layers are electromagnetically driven.

[b]Indirectly estimated from references in [23,28].

[c]The authors provide a Reynolds number of approximately 500 based on the rms velocity fluctuations and injection length scale. Furthermore, they explicitly mention that this rms Reynolds number is four to five times larger than that of Jullien *et al.* [27]. We have therefore conservatively estimated the Reynolds number based on the velocity magnitude for the experiments by Rivera and Ecke to be of the order of 1200.

[d]Obtained through personal communications with H. Punzmann (ANU, Australia).

=0.14) corresponds to a shallower fluid-layer geometry than those reported in the literature. The Reynolds numbers based on a characteristic horizontal velocity scale are presented in the last column of Table II. In the present study, the value of the Reynolds number is approximately five times larger than the cited literature values, therefore the dipole experiences less viscous dissipation. The Reynolds numbers of the present experiments are comparable or slightly higher than that of Rivera and Ecke [25]. Note that Rivera and Ecke explicitly mention that, although their Reynolds number (see also footnote *c* in Table II) is four to five times larger than that of Jullien *et al.* [27], considerable finite Reynolds number effects remain, which result in deviations from the theoretical expectations. Similar concerns were also expressed by Boffetta and Sokolov [33] and recently by Lindborg [34].

D. Degree of two-dimensionality of shallow dipoles

Qualitatively the 3D structure of the dipolar vortex in the two-layer fluid shows a great resemblance with that seen in the single-layer configuration. In order to make a more quantitative comparison of the importance of the 3D flow structure of the coherent vortices between the single and two-layer fluids, we will now consider the ratio q of the kinetic energy contained in the vertical motion E_V to that in the horizontal motion E_H, evaluated at a horizontal plane S at mid-depth in the upper layer, defined as

$$q = \frac{2\int\int_S w^2 dxdy}{\int\int_S (u^2+v^2)dxdy}. \tag{4}$$

Note that the horizontal velocity components u and v are measured in the laboratory frame and that a factor two has been introduced in this definition so that for fully developed isotropic turbulence this ratio q would have a value of 1.0. The magnitude of the vertical velocity w is approximately $\sqrt{q}\cdot 100\%$ of the horizontal velocity magnitude $\mathcal{U}$.

Figures 7(a) and 7(b) display the evolution of the kinetic energy ratio q as obtained numerically and experimentally, respectively. It is observed that the ratio q increases during the forcing (i.e., for $0<t\leq 1$ s), attains a global maximum at around $t=2.0$ s, long after the forcing has been switched off, and then decays gradually. Clearly, the kinetic energy ratio decreases with decreasing H_{ul}. For the aspect ratios consistent with Tabeling and co-workers [23,27,28] and Rivera and Ecke [25], typical values of the vertical velocity w amount to 30 or 45% of the horizontal velocity magnitude $\mathcal{U}$. Surprisingly, the typical maximum value of q corresponds with that for the single-layer fluid. Figure 12(b) in [10] shows a maximum q value of approximately 0.25 for $H=9.3$ mm and $j_x=0.11$ A/cm^2 [recomputed with the current definition of q, i.e., Eq. (4)]. Based on the comparison of this ratio q, the degree of three-dimensionality of shallow flows in a two-layer setup is comparable to that in a single-layer setup.

In Fig. 7(b) the experimentally obtained ratio q is presented. Qualitatively, a decrease of kinetic energy ratio q with decreasing H_{ul} is seen and q attains its maximum around $t=2.0$ s. Apart from the initial time behavior (where the noise in the vertical velocity distribution is corrupting the ratio q), a fairly good qualitative agreement is seen with Fig. 7(a). Here, $w\sim 20\%$ of $\mathcal{U}$ for the corresponding literature values of the aspect ratio γ.

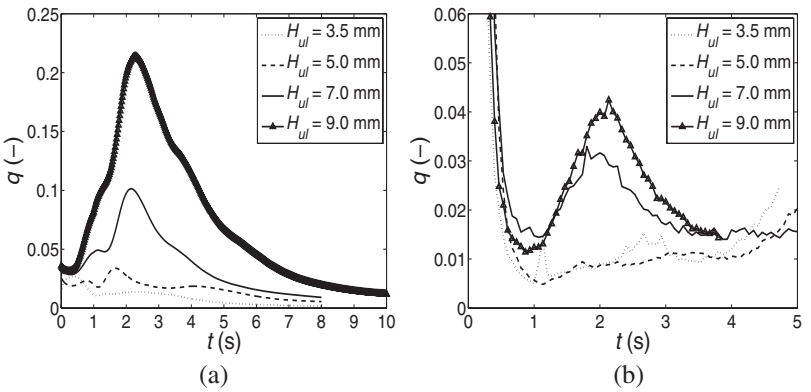

FIG. 7. (a) Numerically obtained evolution of the kinetic energy ratio q with varying upper fluid depth H_{ul}. This ratio is evaluated at a horizontal plane at mid-depth of the upper layer. (b) As (a), but now for the experiments.

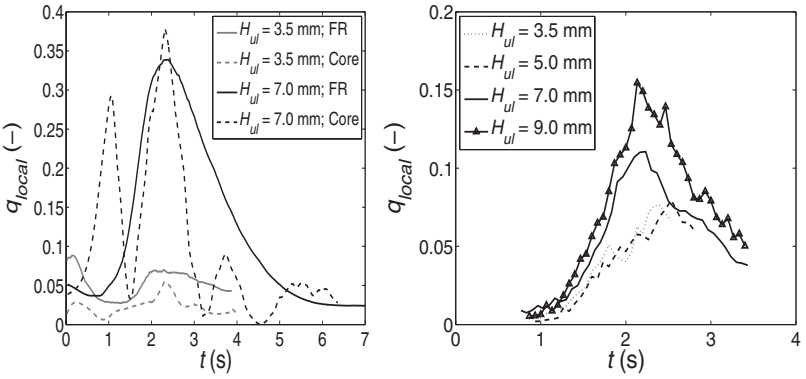

FIG. 8. (a) Numerically obtained evolution of the "local" kinetic energy ratio q_{local} with varying upper fluid-layer depth H_{ul}. This q_{local} is evaluated at two co-moving locations: the frontal side (solid lines) of the dipole [see gray rectangle of Fig. 6(b)], and a small region around the vortex cores (dashed lines). (b) As (a), but now for the experiments evaluated only for a small area near the frontal side of the dipole.

Quantitatively, the difference between the experimentally and numerically obtained kinetic energy ratio q is substantial, which is mainly attributed to the generation of interfacial deformations as indicated in Fig. 5. These interface deformations are intimately linked with the local vertical motion and they extract energy from the dipole, most efficiently when the interface Froude number is of order unity, which is the case in our experiments. The potential energy per unit area contained in such an interfacial deformation is of the order $g\Delta\rho A^2$, where A is the amplitude of the deformation [1]. With the area taken as the dipole area, i.e., $\pi(2D)^2$, and a deformation amplitude estimated of the order of 1 mm, this potential energy turns out to be of the same order as the kinetic energy contained in the vertical motion of the complete upper-fluid layer domain. Therefore, when interface deformations are present, the E_V will most likely be substantially lower than in a simulation without interface deformation, thereby reducing the ratio q in the experiment as compared to the simulations.

The energy ratio q defined by Eq. (4) is a global quantity, while the vertical motions are rather localized in space (see, e.g., Fig. 6). Therefore, one could falsely conclude from the relative low values of the ratio q (as depicted in Fig. 7) that the flow is close to planar, i.e., quasi-two-dimensional. To illustrate the importance of vertical motions, we have additionally calculated the energy ratio according to (4), but now based on a smaller area S, located at the frontal side of the dipole [indicated by the gray rectangle in Fig. 6(b)] or located near the vortex cores. Figure 8(a) presents the numerically obtained evolution for this local ratio q_{local} for both locations, i.e., near the front side of the dipole (solid lines) and near the vortex cores (dashed lines). Furthermore, black indicates H_{ul}=7.0 mm and gray H_{ul}=3.5 mm. Noteworthy is the general increase of this local ratio q_{local} with a factor 3 to 4 with respect to the data displayed in Fig. 7. Locally, the magnitude of the vertical velocity is approximately 70% that of the horizontal velocity magnitude. In Fig. 8(b) the experimentally obtained q_{local}-values are presented (evaluated near the front of the dipole) for decreasing H_{ul}. Besides the general larger value for q_{local} as compared to the ratio q in Fig. 7(b), a general increase of the ratio q_{local} with a factor 4 to 5 with respect to Fig. 7(b) is observed. For the considered range of the aspect ratio γ the vertical velocity component w is 25%–40% that of the horizontal velocity magnitude $\mathcal{U}$. Clearly, the vertical motions are localized in space and global quantities tend to underestimate the importance of 3D motions in the shallow fluid layer.

As discussed in Sec. IV C, the magnitude of the vertical velocity remains approximately constant while the magnitude of the horizontal velocity components increase with decreasing H_{ul} (see Fig. 6), thereby reducing the ratio $q(=E_V/E_H)$ as defined in Eq. (4). Additional simulations have been performed for decreasing upper fluid-layer depths while keeping the magnitude of the horizontal velocity field approximately constant (the Re-value at the end of the forcing phase was kept constant at 1250). It turns out that the ratio q obtained from these simulations shows approximately the same magnitude and evolution as depicted in Fig. 7(a). Therefore, the kinetic energy ratio q depicted in Fig. 7(a) was not biased by the stronger electromagnetic forcing closer to the magnets for decreasing H_{ul}.

In Fig. 9, the numerically obtained normalized horizontal divergence Λ is displayed for three different evaluation levels $z=h$ inside the upper layer (with depth H_{ul}=7.0 mm). This quantity Λ is computed as

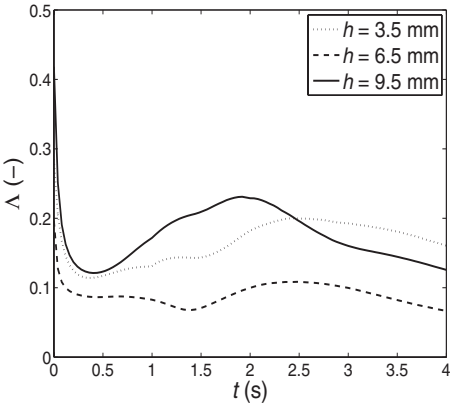

FIG. 9. Numerically calculated evolution of the normalized horizontal divergence Λ at three different evaluation levels ($z=h$ =3.5, 6.5, and 9.5 mm) inside the upper fluid layer (with depth H_{ul}=7.0 mm). Note that H_{bl}=3 mm, thus the evaluation levels 3.5, 6.5, and 9.5 mm correspond to positions 0.5 mm above the internal interface, 3.5 mm above the internal interface (mid-depth of the top layer), and 0.5 mm below the free surface, respectively.

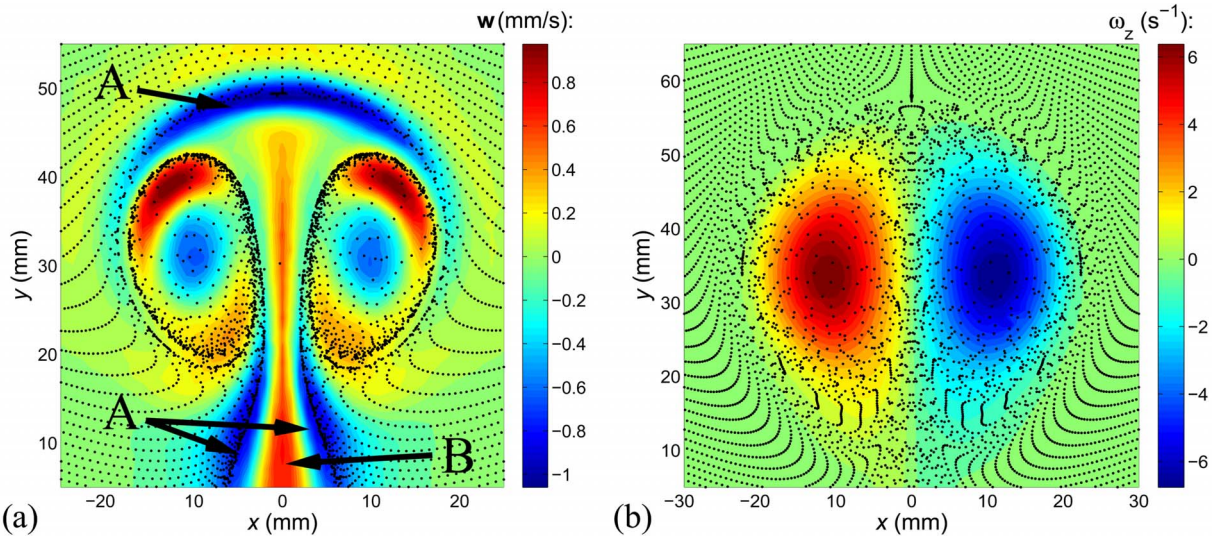

FIG. 10. (Color online) (a) Distribution of tracer particles (black dots) on the free surface of the $H_{ul}=7.0$ mm simulation at $t=3.75$ s. Colors/gray scales indicate the magnitude of the vertical velocity w just below the free surface at $z=9.5$ mm. In these figures, 'A' indicates a region of negative vertical motion (i.e., $w<0$) and 'B' a positive vertical motion ($w>0$). (b) Distribution of tracer particles at $t=3.75$ s obtained with a 2D simulation, where colors/gray scale values indicate the magnitude of the vorticity ω_z. In this subfigure, the left patch contains positive vorticity ω_z and the right one negative vorticity ω_z.

$$\Lambda = \frac{H_{ul}\int\int_S |\nabla_H \cdot \mathbf{v}| dxdy}{D\int\int_S |\omega_z| dxdy}, \tag{5}$$

where ∇_H denotes the divergence with respect to the horizontal components and D the magnet diameter. The normalization factor $D\int\int_S|\omega_z|dxdy$ is a measure of the characteristic horizontal velocity. The normalized horizontal divergence Λ depicted in Fig. 9 is nonzero at all three measurement levels, whereas in purely 2D (incompressible) flow it is exactly zero (by definition). The highest Λ values are observed at the level closest to the free surface ($h=9.5$ mm) and the internal interface ($h=3.5$ mm) as $|\partial w/\partial z|$ attains its maximum there. At approximately mid-depth of the upper fluid layer $\partial w/\partial z$ is approximately zero, leading to low values of the normalized horizontal divergence. After the forcing phase, the magnitude of Λ for the two-layer configuration is smaller than that of the single-layer case [10].

E. Tracer transport at the free surface

To illustrate the effect of the 3D structures inside the shallow fluid layer on motion at the free surface, the transport of massless passive particles is numerically studied. These particles are released at $t=0$ on a uniformly distributed spatial grid (consisting of 9800 particles in total) at the free surface. Although the vertical velocity is identically zero at the free surface, vertical motions inside the flow do influence tracer transport on this surface, since in general $\nabla_H \cdot \mathbf{v} \neq 0$ at the free surface.

In Fig. 10(a) the numerically obtained tracer distribution is shown at $t=3.75$ s for the 3D simulation (with $H_{ul}=7.0$ mm), where colors indicate the magnitude of the vertical velocity just below the surface (at $z=9.5$ mm) and particle positions by the black dots. As $w=0$ at the free surface, the tracer particles are bound to the surface and therefore may accumulate locally. It is clearly seen that the particles become concentrated in narrow bands coinciding with the presence of downward vertical motion below the surface, both at the front and tail side of the dipole. Higher particle concentrations are thus observed in regions where the horizontal flow field is convergent, whereas lower concentration corresponds to locally $\nabla_H \cdot \mathbf{v} < 0$. Note that the normalized horizontal divergence Λ [see Fig. 9] attains its maximum close to the free surface.

The horizontal velocity field of an incompressible 2D flow is by definition divergence-free and narrow bands of accumulated particles will therefore not form in this case. This is illustrated by the 2D simulation in Fig. 10(b), where a fairly uniform particle distribution is observed. Clearly, caution is needed when interpreting passive tracer transport and dispersion at the free surface of these shallow two-layer setups.

V. CONCLUSION

The canonical laboratory setup to study nonrotating 2D turbulence is the electromagnetically driven flow in shallow fluid layers. In the last years, this standard laboratory setup utilized a stable two-fluid layer configuration, with the flow measurements performed at the free surface of the upper layer. This top layer is shielded from the no-slip bottom by a denser fluid layer, thus, attempting to minimize the influence of the no-slip bottom on the development of the flow. The question whether this two-layer setup is a significant improvement over the single-layer setup has hardly received any attention.

In this paper, the 3D structures developing in the top layer of a two-fluid layer setup have been examined, both experimentally and with numerical simulations for the generic case of a dipolar flow in a two-layer fluid. Remarkably, these 3D structures and their evolution show a close resemblance with those observed in a single fluid layer. Even for the smallest upper fluid layer thickness (whose geometrical aspect ratio is significantly lower than values of previously reported experimental studies on 2D turbulence utilizing a two-layer fluid) the same 3D structures emerge as in the single-layer fluid.

With the aid of the numerical simulations it is shown indirectly that the development of the frontal circulation is related to deformations of the internal interface. In contrast to more qualitative studies reported in the literature, the frontal circulation has been observed in all the performed two-fluid layer experiments.

Quantities used as indicators for quasi-2D flow behavior, i.e., the ratio (q) of kinetic energy contained in the vertical motion to horizontal motion and the normalized horizontal divergence (Λ), show a similar evolution and quantitative behavior as that was previously seen for the same dipolar flow in a shallow single fluid-layer. Based on our observations of the kinetic energy ratio q, the two-layer configuration does not provide a significant improvement over the single-layer setup. Furthermore, passive tracer transport at the free surface shows the emergence of distinct narrow bands of particles, which are related to the nonzero horizontal divergence. As 2D flow is by definition horizontally divergence-free, such narrow bands do not develop in the purely 2D case. Since the vortex dipole can be considered as a generic flow structure in 2D turbulence, the conclusions of the present study may apply more generally to experimental realizations of 2D turbulence, both for the decaying and the forced case.

ACKNOWLEDGMENTS

This work is part of the Research Program No. 36 "Two-Dimensional Turbulence" of the "Stichting voor Fundamenteel Onderzoek der Materie (FOM)," which is financially supported by the "Nederlandse Organisatie voor Wetenschappelijk Onderzoek (NWO)."

[1] P. K. Kundu, *Fluid Mechanics* (Elsevier, Amsterdam, 2004).
[2] G. H. Jirka, J. Hydraul. Res. **39**, 567 (2001).
[3] W. S. J. Uijttewaal and G. H. Jirka, J. Fluid Mech. **489**, 325 (2003).
[4] J. Sommeria, J. Fluid Mech. **170**, 139 (1986).
[5] N. F. Bondarenko, M. Z. Gak, and F. V. Dolzhanskii, Izv. Akad. Nauk SSSR, Fiz. Atmos. Okeana **15**, 1017 (1979).
[6] F. V. Dolzhanskiy, Izv. Akad. Nauk SSSR, Fiz. Atmos. Okeana **23**, 262 (1987).
[7] P. Tabeling, S. Burkhart, O. Cardoso, and H. Willaime, Phys. Rev. Lett. **67**, 3772 (1991).
[8] F. V. Dolzhanskii, V. A. Krymov, and D. Yu. Manin, J. Fluid Mech. **241**, 705 (1992).
[9] R. A. D. Akkermans, L. P. J. Kamp, H. J. H. Clercx, and G. J. F. van Heijst, Europhys. Lett. **83**, 24001 (2008).
[10] R. A. D. Akkermans, A. R. Cieslik, L. P. J. Kamp, R. R. Trieling, H. J. H. Clercx, and G. J. F. van Heijst, Phys. Fluids **20**, 116601 (2008).
[11] H. J. H. Clercx and G. J. F. van Heijst, Appl. Mech. Rev. **62**, 020802 (2009).
[12] H. J. H. Clercx, G. J. F. van Heijst, and M. L. Zoeteweij, Phys. Rev. E **67**, 066303 (2003).
[13] B. Jüttner, D. Marteau, P. Tabeling, and A. Thess, Phys. Rev. E **55**, 5479 (1997).
[14] J. Paret, D. Marteau, O. Paireau, and P. Tabeling, Phys. Fluids **9**, 3102 (1997).
[15] S. Lardeau, S. Ferrari, and L. Rossi, Phys. Fluids **20**, 127101 (2008).
[16] M. P. Satijn, A. W. Cense, R. Verzicco, H. J. H. Clercx, and G. J. F. van Heijst, Phys. Fluids **13**, 1932 (2001).
[17] L. C. Lin, M. Ozgoren, and D. Rockwell, J. Fluid Mech. **485**, 33 (2003).
[18] D. Sous, N. Bonneton, and J. Sommeria, Phys. Fluids **16**, 2886 (2004).
[19] D. Sous, N. Bonneton, and J. Sommeria, Eur. J. Mech. B/Fluids **24**, 19 (2005).
[20] H. P. Greenspan, *The Theory of Rotating Fluids* (Cambridge University Press, London, 1969).
[21] U. T. Bödewadt, Z. Angew. Math. Mech. **20**, 241 (1940).
[22] A. R. Cieślik, R. A. D. Akkermans, L. P. J. Kamp, H. J. H. Clercx, and G. J. F. van Heijst, Eur. J. Mech. B/Fluids **28**, 397 (2009).
[23] J. Paret and P. Tabeling, Phys. Rev. Lett. **79**, 4162 (1997).
[24] G. Boffetta, A. Cenedese, S. Espa, and S. Musacchio, EPL **71**, 590 (2005).
[25] M. K. Rivera and R. E. Ecke, Phys. Rev. Lett. **95**, 194503 (2005).
[26] D. Marteau, O. Cardoso, and P. Tabeling, Phys. Rev. E **51**, 5124 (1995).
[27] M.-C. Jullien, J. Paret, and P. Tabeling, Phys. Lett. **82**, 2872 (1999).
[28] M.-C. Jullien, P. Castiglione, and P. Tabeling, Phys. Lett. **85**, 3636 (2000).
[29] M. G. Shats, H. Xia, H. Punzmann, and G. Falkovich, Phys. Rev. Lett. **99**, 164502 (2007).
[30] E. A. Gak and G. R. Rik, Dokl. Akad. Nauk SSSR **175**, 856 (1967).
[31] M. Raffel, C. E. Willert, and J. Kompenhans, *Particle Image Velocimetry: a Practical Guide* (Springer, Berlin, 1998).
[32] C. Snyder, R. Plougonven, and D. J. Muraki, J. Atmos. Sci. **66**, 3464 (2009).
[33] G. Boffetta and I. M. Sokolov, Phys. Fluids **14**, 3224 (2002).
[34] E. Lindborg, Phys. Rev. Lett. **102**, 149401 (2009).